Optimizing Self-Consistent Field Theory Block Copolymer Models with X-Ray Metrology

Adam F. Hannon[a†], Daniel F. Sunday[a], Alec Bowen[b], Gurdaman Khaira[c], Jiaxing Ren[b], Paul F. Nealey[b,d], Juan J. de Pablo[b,d], R. Joseph Kline[a‡]

a Materials Science and Engineering Division, National Institute of Standards and Technology, 100 Bureau Drive, Gaithersburg, MD 20899

b Institute for Molecular Engineering, University of Chicago, 5801 S Ellis Ave, Chicago, IL 60637

c Mentor Graphics, 8005 Boeckman Rd, Wilsonville, OR 97070

d Argonne National Laboratory, 9700 Cass Ave, Lemont, IL 60439

Electronic Supplementary Information (ESI):

ESI1 Interface Model and Shape (Trapezoid & Grid) Models

i. Interface Model

A model of the interface width is necessary to calculate the Debye-Waller factor in the intensity calculations. The self-consistent field theory (SCFT) model can be used to extract such an interface width by fitting the normalized density profile ϕ_- produced by the calculations to a function that characterizes the interface width. One such function commonly used is the error function such that $\phi_-(x) = \mathrm{Erf}\left(\frac{x-\mu_x}{\sigma\sqrt{2}}\right)$, where x is the position along the density profile perpendicular to the interface that is used for fitting, μ_x is the center of the interface between the two blocks, and σ is interface width w_{Int}. Using such a model, a fitting procedure can be introduced to find σ given a density profile ϕ_- from the SCFT calculations with a known μ_x. However, the interface width is spatially variant and thus for an accurate measure of the interface width this procedure would have to be performed across different cross-sections of the interface in the 2D simulations. Instead, the bulk interface width as a function of χN can be calculated to produce a reference curve. Such a reference curve was produced and is shown in Figure S1a. To avoid dependencies on N, the interface width is plotted normalized by copolymer period L_0. In addition to the SCFT fit curve, the simple model of $w_{\mathrm{Interface}} = 2b/\sqrt{6\chi}$ and that of $w_{\mathrm{Interface}} = \frac{2b}{\sqrt{6\chi}}\left(1 + \left(\frac{24}{\pi^2\chi N}\right)^{\frac{1}{3}}\right)$ are also plotted (green and red, respectively). They are

†Guest Researcher
‡Address correspondence to joe.kline@nist.gov

normalized by the SSL value of $L_0 = b\chi^{1/6}N^{2/3}$. The second of these models has been used to account for deviations in the interfacial width in the lower χN values of the SSL regime[1,2].

As seen in the Figure, the SCFT values follow most closely with the second model, underestimating it by a certain fraction which is plotted in Figure S1b. The simple inverse square root model gives the lowest interface values. The real copolymer system is expected to have larger interface widths than the SCFT model produced because of fluctuation effects not explicitly captured. Since the second model gives larger interface values than the SCFT model and is an easier way of calculating the interface width used to then calculate DW, the model was chosen to calculate the interface width. Although this interface model is not completely valid at the χN values of the samples examined in this study, it approximates the interface width to first order. The main effect fluctuations have on the interface width is to increase it, so using the second model with the slightly higher interface widths than the SCFT model makes the most sense.

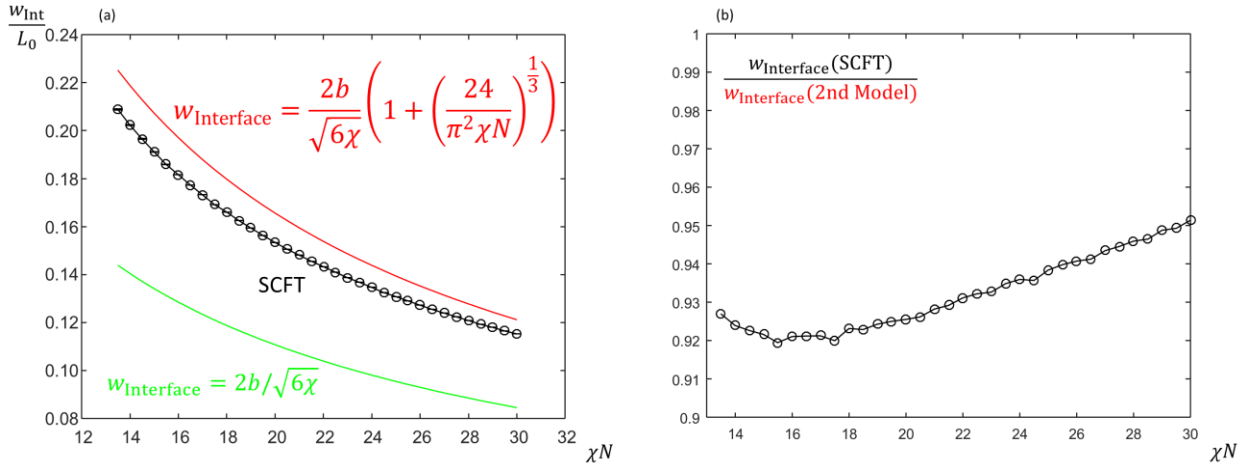

Figure S1: (a) Plot of different interface width models versus χN normalized by L_0. The green curve is a simple inverse square root dependency on χ which greatly underestimates the interface width. The red curve is based on the equation inset in red. The black curve is found from fitting error functions to bulk SCFT calculation density profiles, where the circles represent data points that were fit. (b) A plot of for the SCFT model vs the red model in a.

ii. Shape (Trapezoid & Grid) Models

In addition to the physics based SCFT model, fits to the intensity profiles for the different samples were performed using both a trapezoid and a grid based shape model. These models are useful because the time to perform a single iteration of the Covariance Matrix Adaptation Evolutionary Strategy (CMAES) algorithm is a couple of orders of magnitude faster than using the SCFT grid since each SCFT simulation takes on the order of 10 min to 20 min to perform

while the Fourier transform calculations of the SLD only takes on the order of seconds depending on how many trapezoids and grid points make up the structure (i.e. how highly parameterized the structure is) as the analytical Fourier transform scales linearly with the number of grid points and q data points used (a single grid point at one q data point takes less than a ms to calculate depending on processor speed). Details of the trapezoid model are provided in prior work[3–5].

The grid based shape model uses the same N_{Z} by N_{X} grid resolution as the SCFT simulations and thus should be better suited to directly compare with the structures found from the SCFT than the trapezoid model. A schematic of how the parameters of the grid model are used to produce the SLD density is shown in Figure S2. The grid based shape model considers the template (both neutral brush and crosslinked polystyrene (X-PS) mat regions) the same as in the SCFT model. The major difference in the model is the free region (cyan region in Figure 2 in the main text) where the polymer density fields evolve in the SCFT are replaced with variable shape columns defined by a minimum of 4 parameters, a top width, mid-width(s), bottom width, and mid-width position offset(s). Any number of mid-widths can be used for more complex column shapes. These columns represent the PS lamella and the interstitial regions define the poly(methyl methacrylate) (PMMA) lamella. The samples examined have a $P_{\mathrm{Temp}}/L_0 = 3$, so the assumption is made 1 column has its own independent shape parameters (referred to as the guide stripe column) and the other two columns have the same shape parameters by symmetry (referred to as the brush columns). The horizontal position of the columns relative to the underlying template is normally fixed with the guide stripe column centered over the X-PS mat and the two brush columns centered around the center of the of brush region. To test a U-type structure over the guide stripe, the brush columns are shifter over the guide stripe instead and the guide stripe column centered over the brush region. Between the four template parameters L_{GS}, L_{Bot}, t_{GS}, and t_{Br}, the film thickness t_{Film}, the minimum of 8 column shape parameters, and the 3 intensity scaling parameters, the grid based shape model has at least 16 parameters to optimize. However, since the model creates a grid shape orders of magnitude faster than a single SCFT simulation, potential shape solutions can be found in minutes rather than on the order of days for a full optimization thus making the use of such a model for calibration and comparative purposes very useful. Once regions are defined by the geometric parameters in the model, the assigned scattering length density (SLD) values in that region in the grid are round based on whether or not the assigned region falls within an acceptable margin of the length scales defined for the

feature under question using a prescribed rounding algorithm. Note in the model since no fundamental length scale needs to be optimized like L_0 must be in the SCFT simulations, P_{Temp}, the template period, is fixed.

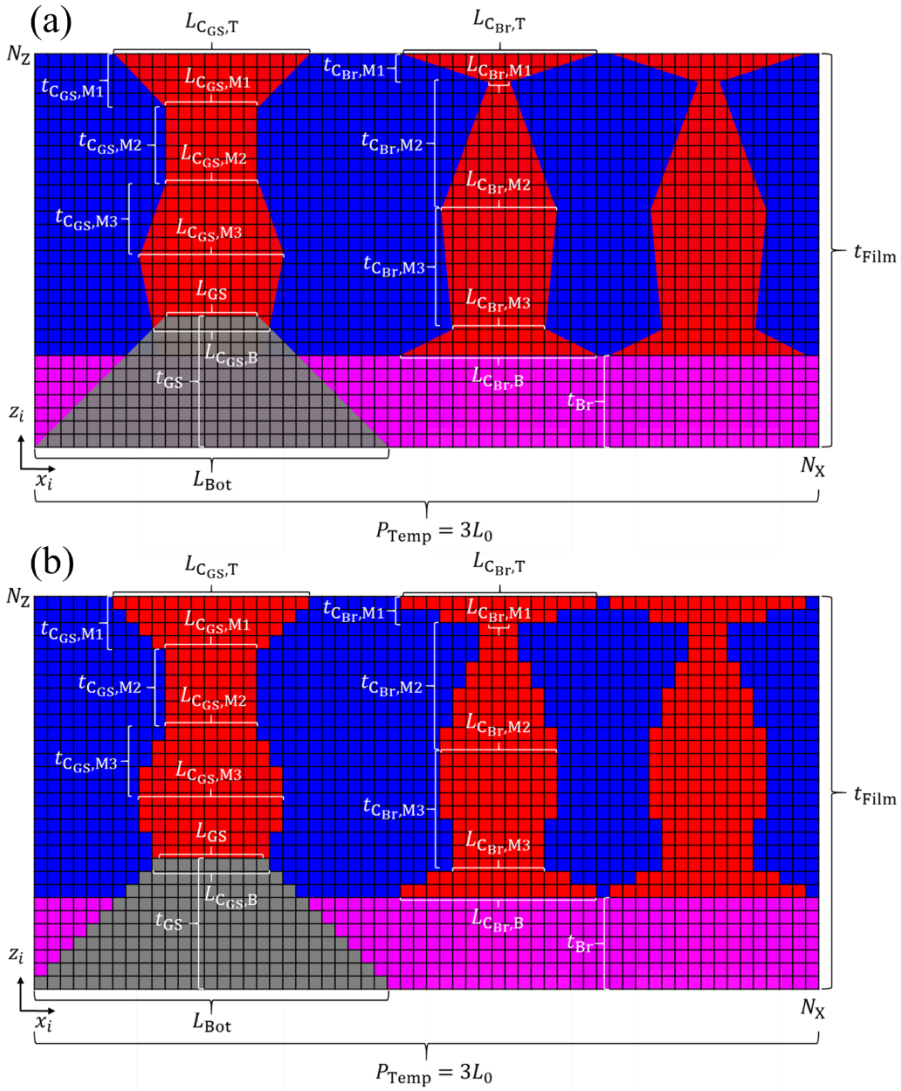

Figure S2: Schematic of how the shape parameters are applied to produce the *SLD* used to calculate the simulated intensity profiles in the grid model. (a) shows the outline of the applied equivalent trapezoid shape model and (b) shows how the grid model appears after rounding of applied parameters has occurred. There are N_Z grid points in the vertical direction and N_X grid points in the horizontal direction. The grey area represents the X-PS guide stripe where the assumption is made the guide stripe is a symmetric trapezoidal area defined by a base width of L_{Bot}, a top width of L_{GS}, and height of t_{GS}. The magenta area defines the neutral brush region where the area is defined by a height parameter t_{Br} and the area between the guide stripe area in the rest of the unit cell. Two distinct sets of column parameters define the three red PS columns in the system. The column over the guide stripe is defined by a top width $L_{C_{GS},T}$, a series of mid-width offsets $t_{C_{GS},Mi}$, a series of mid-widths $L_{C_{GS},Mi}$, and a bottom width $L_{C_{GS},B}$. The column area is defined such that the first set of grid points at the top of the unit cell is defined by $L_{C_{GS},T}$, then a slope is calculated from $t_{C_{GS},Mi}$ and $L_{C_{GS},Mi}$ and used to defined the grid points going down the column for each i mid-width (here 3 total mid-widths are shown), and a final area connecting the column to the guide stripe is defined based on the difference in the total column height for $t_{C_{GS},Mi}$ and t_{GS} from t_{Film} down to $L_{C_{GS},B}$. A similar approach

is used for defining column areas is used for the two columns over the brush but with the constraint those two columns are identical. The columns are centered over the guide stripe for the guide stripe column and around the center for the brush columns, though this constraint can easily be relaxed by adding horizontal offset parameters for the columns. Such a horizontal offset is used with a fixed offset of $0.5L_0$ to model a U-shaped structure that is observed for sample 5. Once the grid is defined, the SLD values are assigned such that the grey area has a value of 0, the red areas have a value of 0, the blue area has a value C_{SF}, and the magenta area has a value of $0.5C_{\mathrm{SF}}$.

Once a SLD profile has been developed, the simulated intensity is calculated as follows:

$$F(\vec{\boldsymbol{q}}) = \int \big(SLD(\vec{\boldsymbol{r}}) * \sigma(x)\big) e^{-i(\vec{\boldsymbol{q}}\cdot\vec{\boldsymbol{r}})} d\vec{\boldsymbol{r}} \tag{S1}$$

The form factor is defined as a function of the SLD and structure factor $\sigma(x)$ in Eqn S1.

$$F(\vec{\boldsymbol{q}}) = \int \big(SLD(\vec{\boldsymbol{r}}) * \textstyle\sum_n \delta(x - nP_{\mathrm{Temp}})\big) e^{-i(\vec{\boldsymbol{q}}\cdot\vec{\boldsymbol{r}})} d\vec{\boldsymbol{r}} \tag{S2}$$

The delta function form of $\sigma(x)$ is substituted into Eqn S1 to get Eqn S2.

$$F(\vec{\boldsymbol{q}}) = \int (SLD(x,z) * \delta(x)) e^{-i(\vec{\boldsymbol{q}}\cdot\vec{\boldsymbol{r}})} d\vec{\boldsymbol{r}} \tag{S3}$$

Taking only the $n = 0$ term since the absolute scaling is not needed, Eqn S3 is obtained. Using the delta function identity for convolutions in Eqn S4, Eqn S5 is obtained:

$$SLD(x,z) * \delta(x) = SLD(x,z) \tag{S4}$$

$$F(q_x, q_z) = \int SLD(x,z) e^{-i(q_x x + q_z z)} dx dz \tag{S5}$$

For the grid, the SLD is defined piecewise as shown in Eqn S6.

$$SLD(x,z) = \begin{cases} 0 \text{ if } x,z \in \text{PMMA domain} \\ 0.5 \text{ if } x,z \in \text{Brush domain} \\ 1 \text{ if } x,z \in \text{PS/X-PS domain} \end{cases} \tag{S6}$$

From this definition, the SLD is constant over the different domain regions. Defining each region in terms of indices x_i and z_i ranging from 1 to N_{X} and 1 to N_{Z}, respectively, of equal lengths l_x and l_z such that $l_x = P_{\mathrm{Temp}}/N_{\mathrm{X}}$ and $l_z = t_{\mathrm{Film}}/N_{\mathrm{Z}}$ and defining $SLD(x,z) = SLD(x_i, z_i)$, $F(q_x, q_z)$ can be written as shown in Eqn S7.

$$F(q_x, q_z) = \textstyle\sum_{x_i=1}^{N_{\mathrm{X}}} \sum_{z_i=1}^{N_{\mathrm{Z}}} \int_{l_z(z_i-1)}^{l_z z_i} \int_{l_x(x_i-1)}^{l_x x_i} SLD(x_i, z_i) e^{-i(q_x x + q_z z)} dx dz \tag{S7}$$

$SLD(x_i, z_i)$ is a constant for every x_i, z_i grid point pair can now be factored out and the double integral split leaving Eqn S8.

$$F(q_x, q_z) = \textstyle\sum_{x_i=1}^{N_{\mathrm{X}}} \sum_{z_i=1}^{N_{\mathrm{Z}}} SLD(x_i, z_i) \int_{l_z(z_i-1)}^{l_z z_i} e^{-iq_z z} dz \int_{l_x(x_i-1)}^{l_x x_i} e^{-iq_x x} dx \tag{S8}$$

The two integrals are the same except for the z or x labels. Solving the z one yields Eqn S9.

$$\int_{l_z(z_i-1)}^{l_z z_i} e^{-iq_z z} dz = i \frac{e^{-iq_z z}}{q_z}\Big|_{l_z(z_i-1)}^{l_z z_i} = \frac{i e^{-iq_z l_z z_i}}{q_z}\big(1 - e^{iq_z l_z}\big) \tag{S9}$$

Using the result of Eqn S9 for both the x and z integrals, Eqn S8 becomes Eqn S10.

$$F(q_x, q_z) = -\sum_{x_i=1}^{N_X}\sum_{z_i=1}^{N_Z} SLD(x_i, z_i)\frac{e^{-iq_z l_z z_i} e^{-iq_x l_x x_i}}{q_z q_x}\left(1 - e^{iq_z l_z}\right)\left(1 - e^{iq_x l_x}\right) \quad \text{(S10)}$$

Once $F(q_x, q_z)$ is calculated using Eqn S10, the intensity can be calculated taking the absolute value squared of $F(q_x, q_z)$, where this is done using the complex conjugate as shown in Eqn S11.

$$I_0(\vec{q}) = |F(q_x, q_z)|^2 = F(q_x, q_z)F^*(q_x, q_z) \quad \text{(S11)}$$

Eqns S10 and S11 are the same form used in calculating the simulated intensities for the SCFT results, the only difference there being how $SLD(x_i, z_i)$ is produced.

Using the trapezoid and grid models to simulate the SLD in different optimization runs, optimal fits to the scattered intensity data were produced for sample 1. The resulting *SLD* profiles for the best fits using those models are shown and compared with the best fit using the SCFT model for the same sample in Figure S3a. The corresponding intensity peak slice fits are shown in Figure S3b and c. Examining the intensity peak fits visually, all three models appear to fit the data qualitatively well. To examine their fits more quantitatively, the goodness of fit values Ξ were 0.177 for the trapezoid model, 0.183 for the grid model, and 0.206 for the SCFT model. Both the trapezoid and the grid models had better goodness of fit than the SCFT model, implying there are elements to the average shape profile the SCFT model is missing. Comparing SLD profiles of the grid model and SCFT profile, the biggest differences in the structure occur around the guide stripe shape. The guide stripe region from the grid model solution is larger than the SCFT solution and the bottom of the guide stripe PS column necks more right above the guide stripe. Since the calculations do not distinguish the SLD between the PS lamellae regions and the guide stripe X-PS, the possibility exists that the more complex shape observed near the guide stripe might actually be part of the guide stripe itself rather than the PS lamellae. This means a more complex template model might be necessary to capture the exact shape profile in the SCFT model. Another minor difference occurs near the top surface where the trapezoid model results had a very noticeable wetting layer with the PS domains, the SCFT model had somewhat of a noticeable wetting layer, and the grid model being least discernable in this feature. PS and PMMA should have nearly identical surface free energies, so these wetting layer features could be due to the assumed flat top surface, but if there were any slight preferential wetting the PS layer would be the block for that to occur with it having a slightly lower surface free energy than PMMA, so the results are at least consistent with the block that would be

expected to wet the air surface more. The previous trapezoid study also conducted NEXAFS experiments that indicated 70 % to 80 % of the top surface was PS[3], so this gives more credence to the SCFT model also showing such wetting behavior.

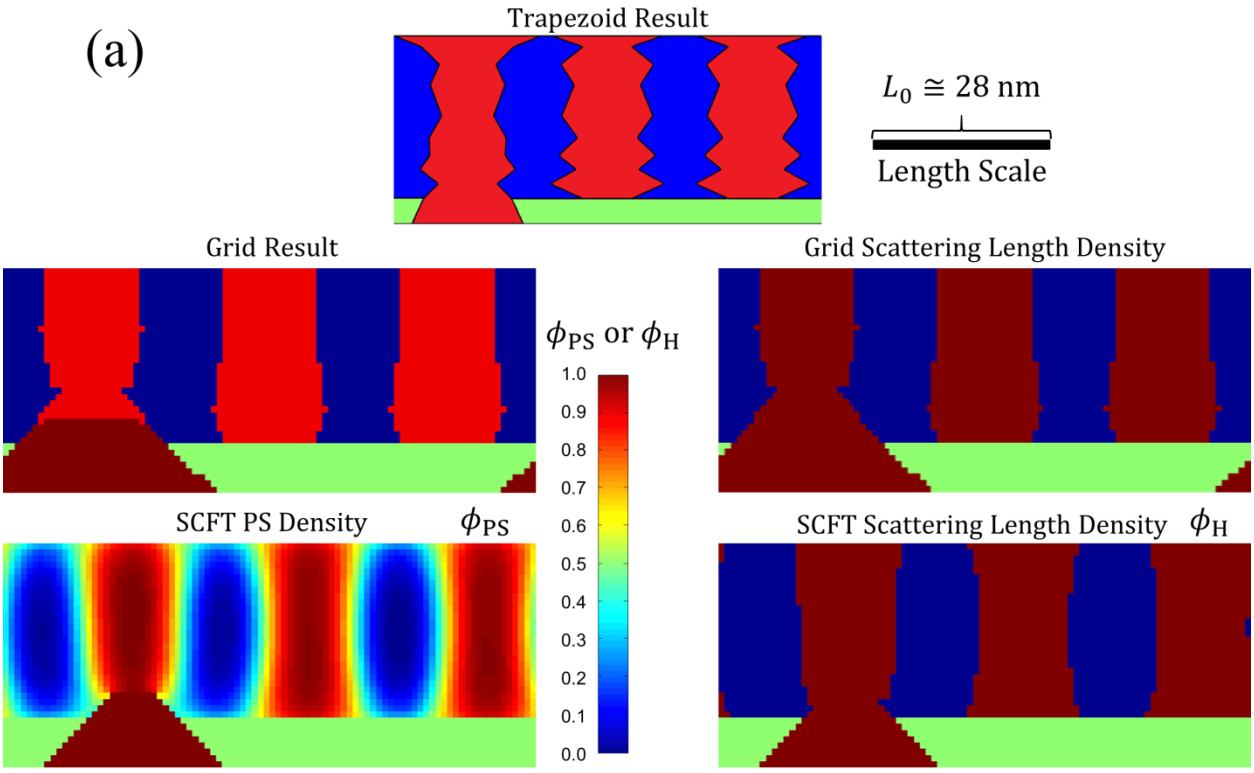

Figure S3a: Resulting scattering length density profiles for the best fits found to the intensity profile for sample 1 from the main text. The trapezoid model (top) uses three columns of ten trapezoids to model the PS *SLD*. The grid model (middle) uses a grid of size N_Z by N_X analogous to the SCFT model where three columns of trapezoidal features are converted to grid shapes as shown in Figure S2 to model the *SLD*. The left image distinguishes the template region which is modeled the same in the SCFT and the BCP region which is modeled more like the trapezoid model. The SCFT model (bottom) best fit results show both the SCFT density profile on the left and *SLD* profile on the right. The length scale bar is for both horizontal and vertical directions (i.e., the aspect ratio as shown is unity).

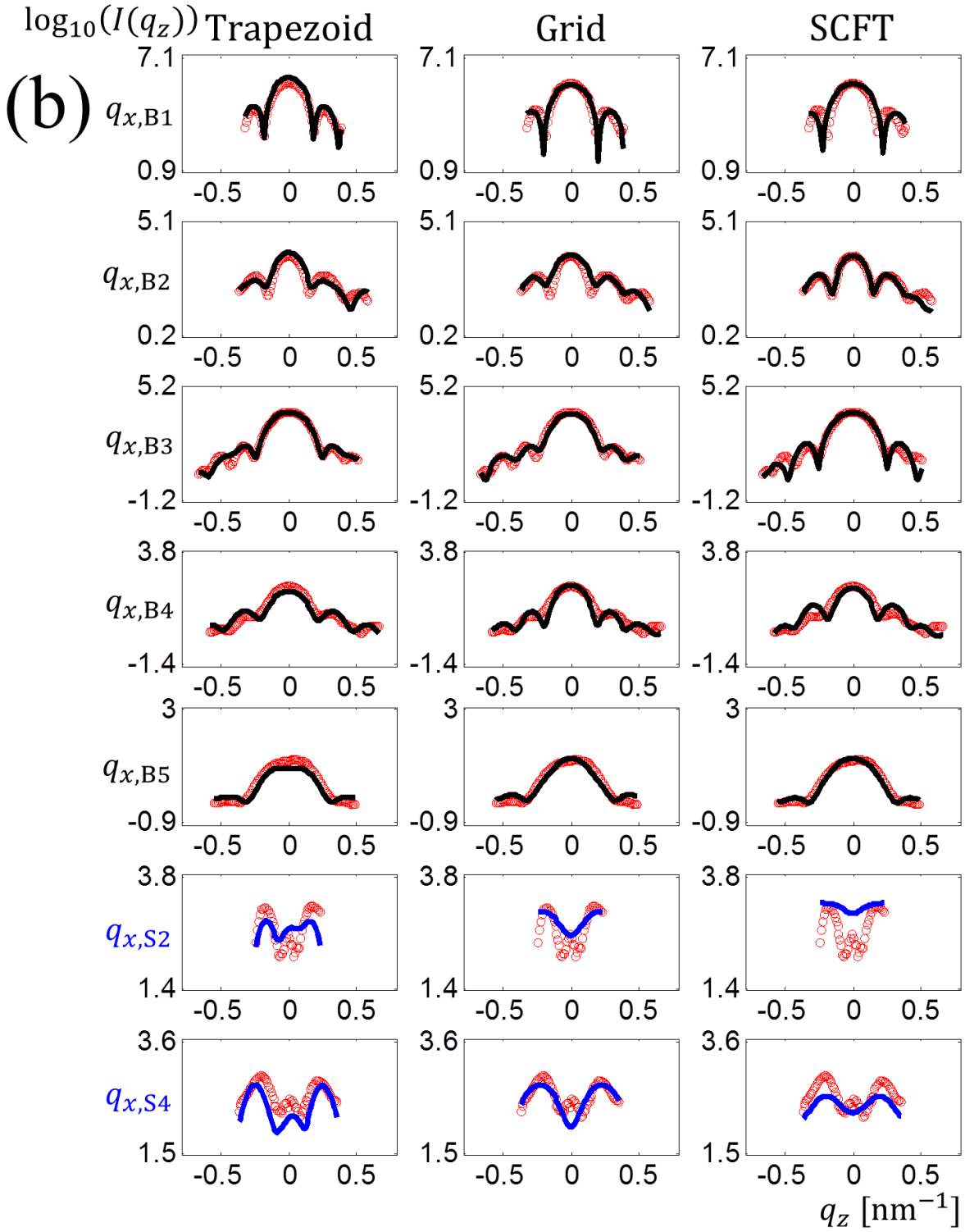

Figure S3b: Best fit scattered intensity profiles for the three models (trapezoid, grid, and SCFT left to right) with Bragg peak slices in black and satellite peak slices in blue plotted over the experimental data (red circles) against q_z.

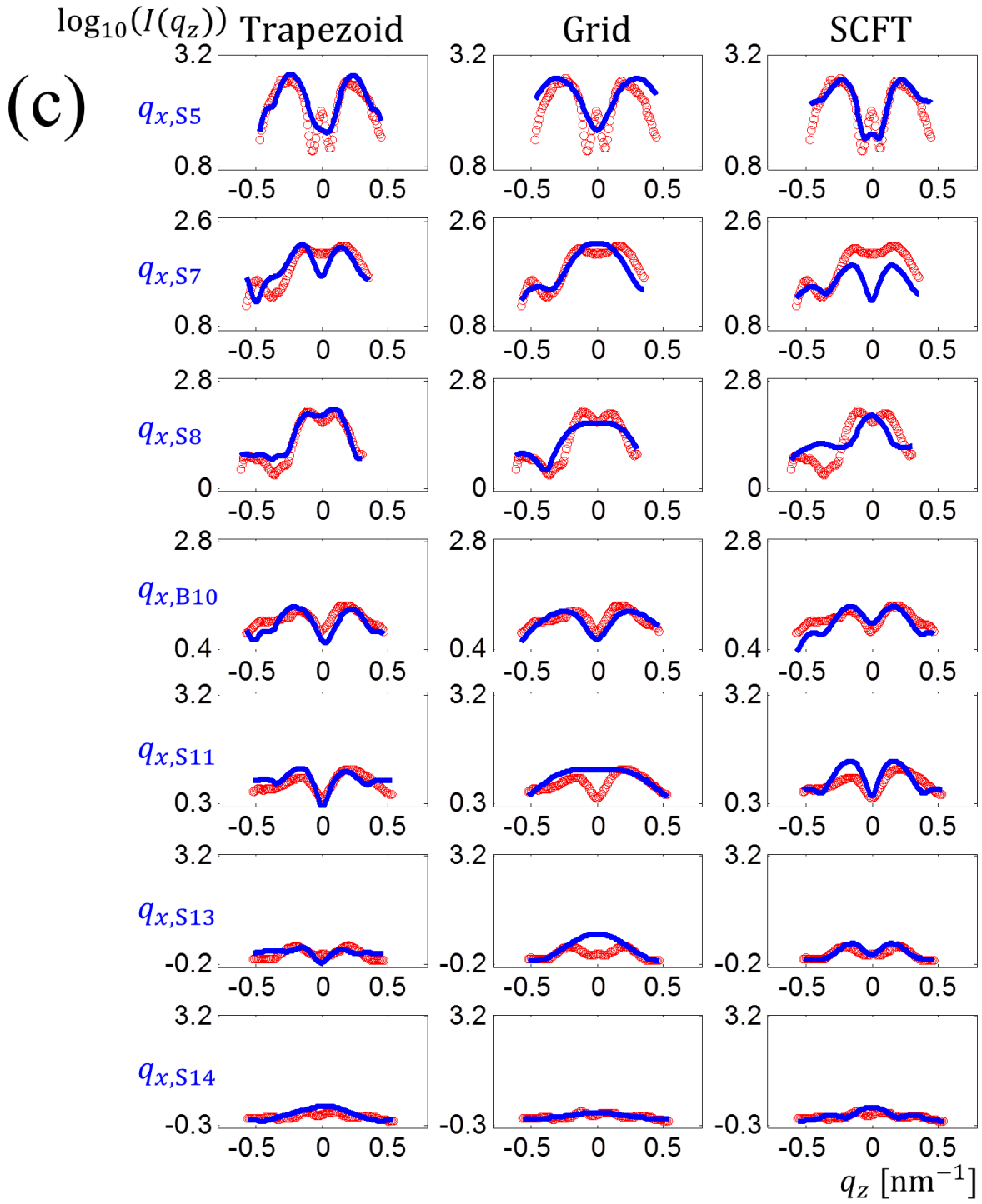

Figure S3c: Best fit scattered intensity profiles for the three models (trapezoid, grid, and SCFT left to right) with satellite peak slices in blue plotted over the experimental data (red circles) against q_z.

ESI2 Simulated Target Structure Study

In order to ensure the inverse methodology works for the SCFT simulations, a test structure was used to create a simulated intensity profile. For this structure, the SCFT parameters

that produced the structure were selected based on values that should match well with a hypothetical experimental set of conditions based on previous knowledge. The parameters used for the test structure are given in Table S1 and the corresponding calculated SCFT density map $\phi_{\mathrm{Tar,PS}}$ and SLD $\phi_{\mathrm{Tar,H}}$ are shown in Figure S4a. A simulated intensity profile for $\phi_{\mathrm{Tar,H}}$ was calculated and Poisson noise was added to its corresponding intensity profile assuming three different values for the minimum intensity $I_{\mathrm{Min}} = 1/\eta$ in terms of the noise parameter η. The added noise is then

$$\zeta(\vec{q}) = \sqrt{\eta I_{\mathrm{Tar}}(\vec{q})}\mathrm{rand}([-1,1]). \quad \text{(S12)}$$

Parameter	Value	Bounds	No Noise	$\eta = 0.1$	$\eta = 0.333$	$\eta = 2$
f	0.44	[0.35:0.52]	0.441 ± 0.004	0.443 ± 0.005	0.445 ± 0.002	0.440 ± 0.001
χN	25.00	[15.0:35.0]	24.6 ± 0.4	24.7 ± 0.3	24.5 ± 0.1	25.0 ± 0.1
t_{Film}/L_0	1.40	[1.30:1.60]	1.37 ± 0.01	1.37 ± 0.01	1.37 ± 0.01	1.37 ± 0.01
L_{GS}/L_0	1.00	[0.35:1.25]	0.95 ± 0.05	0.93 ± 0.10	0.91 ± 0.12	0.92 ± 0.10
L_{Bot}/L_0	1.90	[0.35:2.90]	1.88 ± 0.02	1.87 ± 0.01	1.89 ± 0.01	1.88 ± 0.01
t_{GS}/L_0	0.267	[0.05:0.50]	0.263 ± 0.007	0.263 ± 0.009	0.269 ± 0.004	0.272 ± 0.002
t_{Br}/L_0	0.167	[0.05:0.40]	0.166 ± 0.00**2**	0.172 ± 0.004	0.168 ± 0.004	0.171 ± 0.006
DW	2.50	[1.95:3.48]	2.503 ± 0.001	2.501 ± 0.001	2.501 ± 0.001	2.515 ± 0.001
I_{Exp}	-2.00	[-2.5:-1.5]	-1.997 ± 0.001	-1.998 ± 0.001	-1.999 ± 0.001	-1.989 ± 0.001
I_{Bk}	0.50	[0.11:0.90]	0.500 ± 0.001	0.490 ± 0.002	0.505 ± 0.001	0.900 ± 0.001
Goodness of Fit			No Noise	$\eta = 0.1$	$\eta = 0.333$	$\eta = 2$
		Ξ	0.0193 ± 0.0006	0.0561 ± 0.0001	0.0983 ± 0.0001	0.1670 ± 0.0001

Table S1: The parameters used in the simulated structure study with their actual input values and bounds during fitting on the left and the average fitted values using the CMAES algorithm on the right with their standard uncertainty for the four noise level cases. Average goodness of fit values Ξ are reported at the bottom for the different noise level fits with their standard uncertainty for runs that converged to approximately the lowest observed value. $\Omega_{\mathrm{GS}}, \Omega_{\mathrm{Br}}, \Omega_{\mathrm{Air}},$ and Ω_{SW} were all fixed to values of -7.5, -3, -2, and 7.5, respectively for these test runs.

Fits using the CMAES algorithm were performed for each noise profile and the structures for the best fits found in terms of Ξ are shown in Figure S4a for all the noise levels tested in terms of PS density and SLD. To compare the fits, the goodness of fit parameter Ξ was used to judge how well the inverse methodology worked on a given data set of fixed Poisson noise. Plots

of the fit intensities (log scale) versus q_z against the simulated data are shown in Figure S4b and c going from low noise to high noise from left to right in each column with the left column having the Bragg peaks slices and first three satellite peak slices and the right column the last eight satellite peak slices.

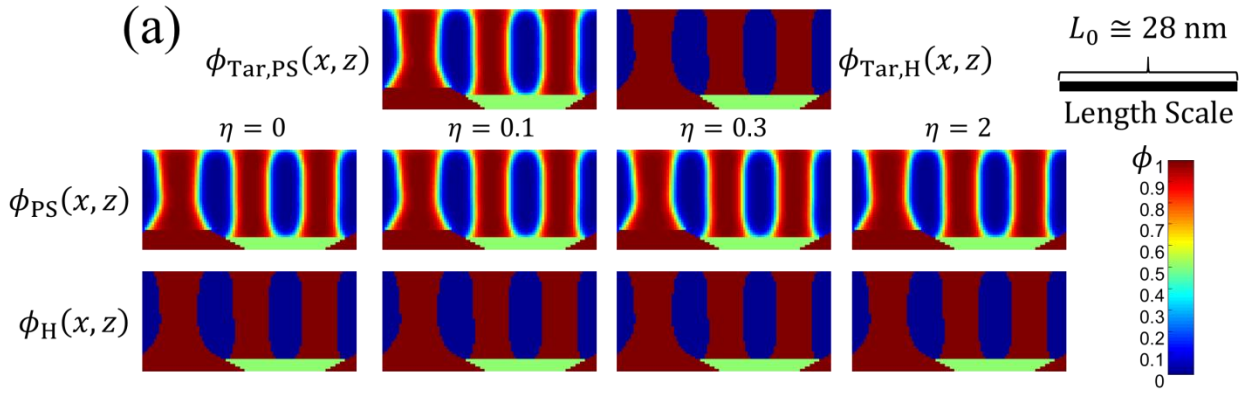

Figure S4a: (Top) The simulated target structure x and z position dependent PS SCFT density profile $\phi_{\mathrm{Tar,PS}}$ (left) and the corresponding converted scattering length density profile $\phi_{\mathrm{Tar,H}}$(right) where blue colors represent PMMA regions, red colors PS and X-PS regions, and green colors brush regions. (Bottom) The PS SCFT density profile ϕ_{PS} best fit for the four Poisson noise levels added to the simulated intensities (left to right increasing noise) and the corresponding scattering length density for each noise level ϕ_{H}. The length scale bar is for both horizontal and vertical directions (i.e., the aspect ratio as shown is unity).

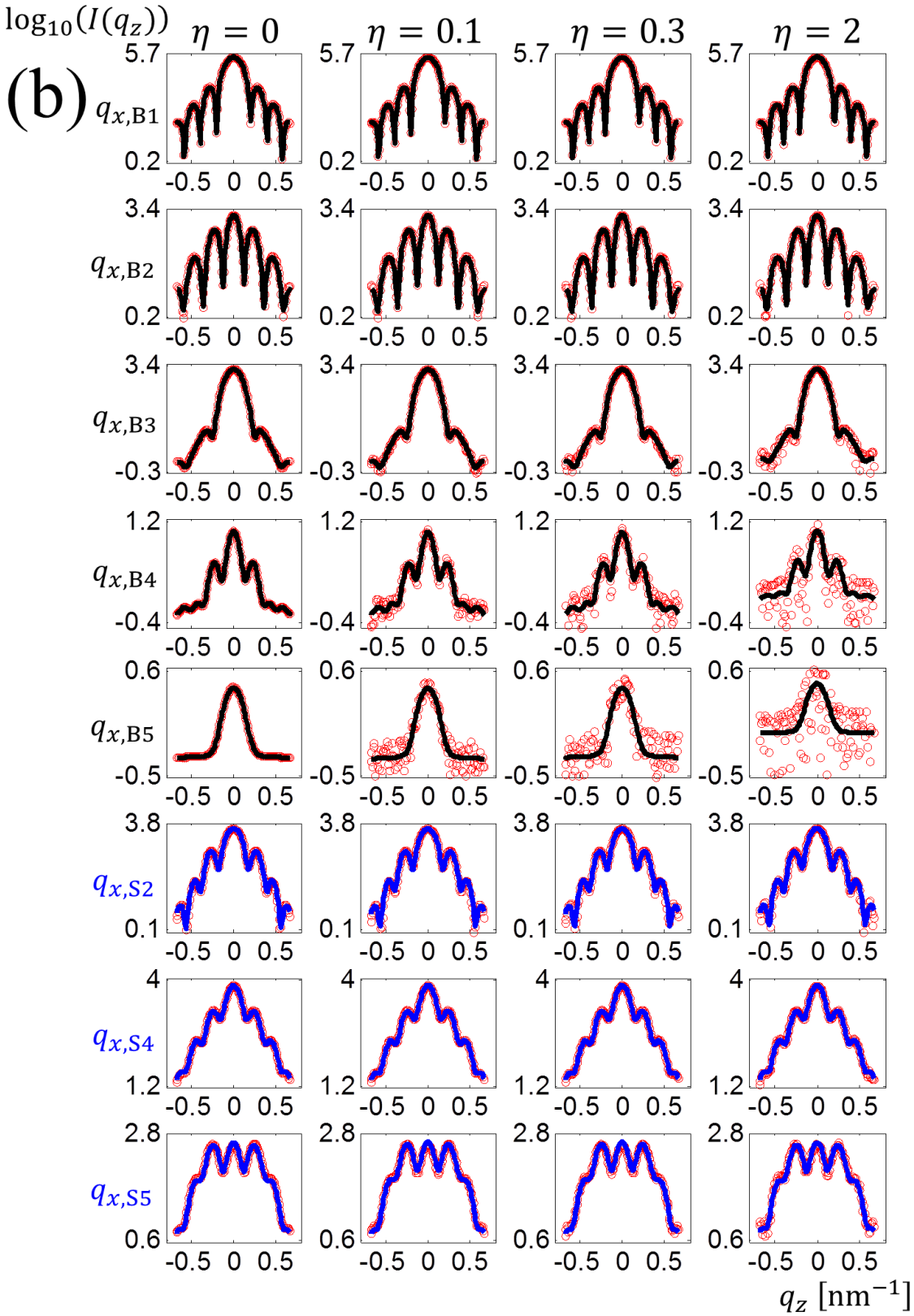

Figure S4b: Plots of the best fit log scale intensity peak slices $\log_{10}(I(q_z))$ found for the simulated SCFT ϕ_H profiles for the noise levels tested (increasing noise from left to right). Black curves are fits for Bragg peak data and blue curves are fits for satellite peak data. Red circles are the simulated structure data with Poisson noise added.

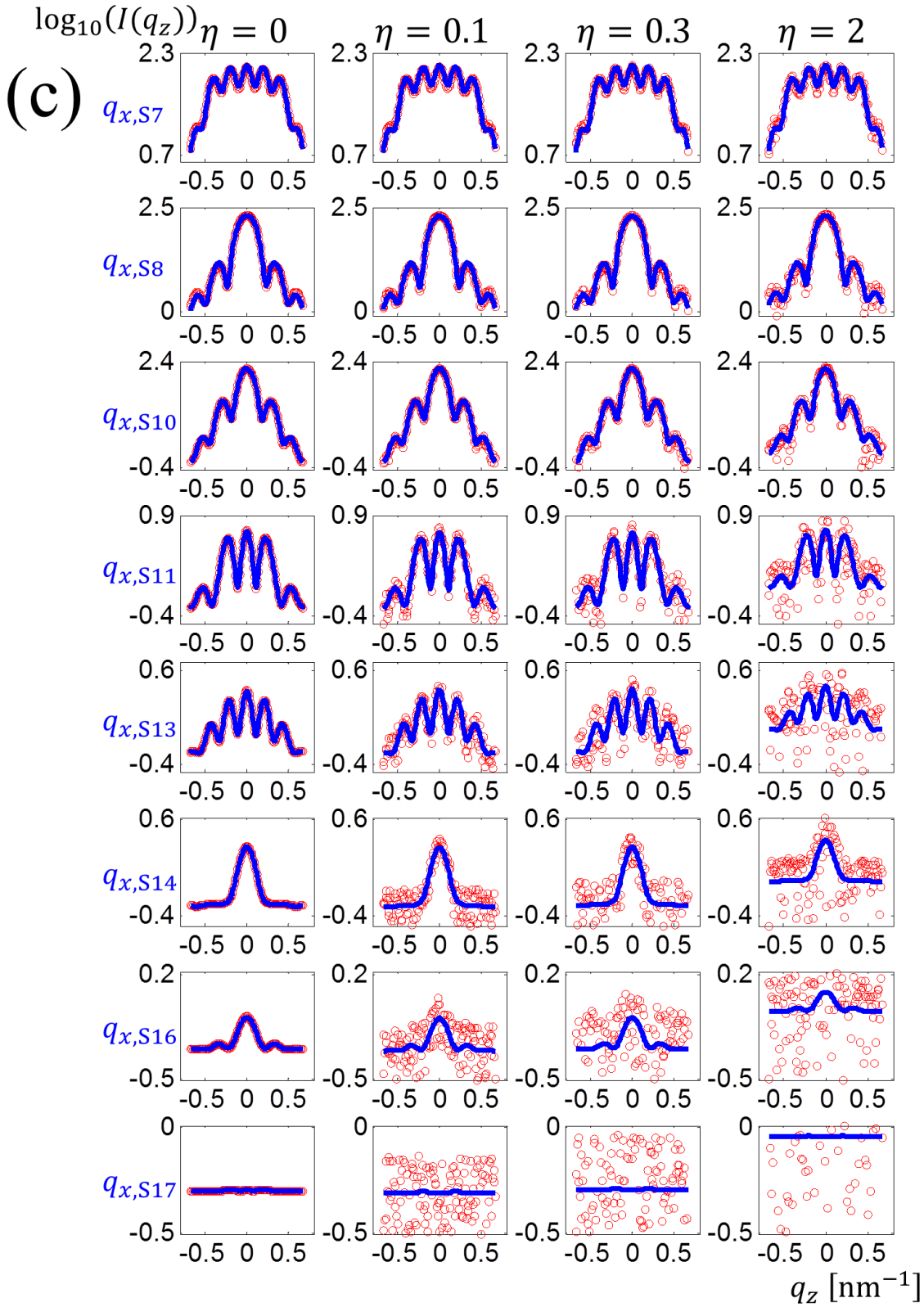

Figure S4c: Plots of the best fit log scale intensity peak slices $\log_{10}(I(q_z))$ found for the simulated SCFT ϕ_H profiles for the noise levels tested (increasing noise from left to right). Blue curves are fits for satellite peak data. Red circles are the simulated structure data with Poisson noise added.

For these structures, all model parameters except Ω_{GS}, Ω_{Br}, Ω_{Air}, and Ω_{SW} were varied with bounds given by Table S1. From preliminary runs, the Ω parameters were found to vary greatly due to the fact a larger range of surface preferentiality conditions gave similar shape profiles, so those parameters were fixed in this study. Three independent runs were performed for each level of noise including the no noise case. As expected, the noisiest cases had the worst fits in terms of Ξ increasing with larger noise as well as having the worst matches in the parameters. With one exception at the highest noise case, all parameters were able to be found within reasonable uncertainty, demonstrating that the CMAES algorithm is robust enough to search the parameter space necessary to fit this kind of scattering data assuming the experimental intensity is produced from a singular periodic contributing structure profile.

ESI3 Satellite Peak Slice Fits

Figure S5a and b shows the satellite peak slice fits for the 5 different guide stripe width samples whose Bragg peak slice fits are shown in Figure 4 of the main text.

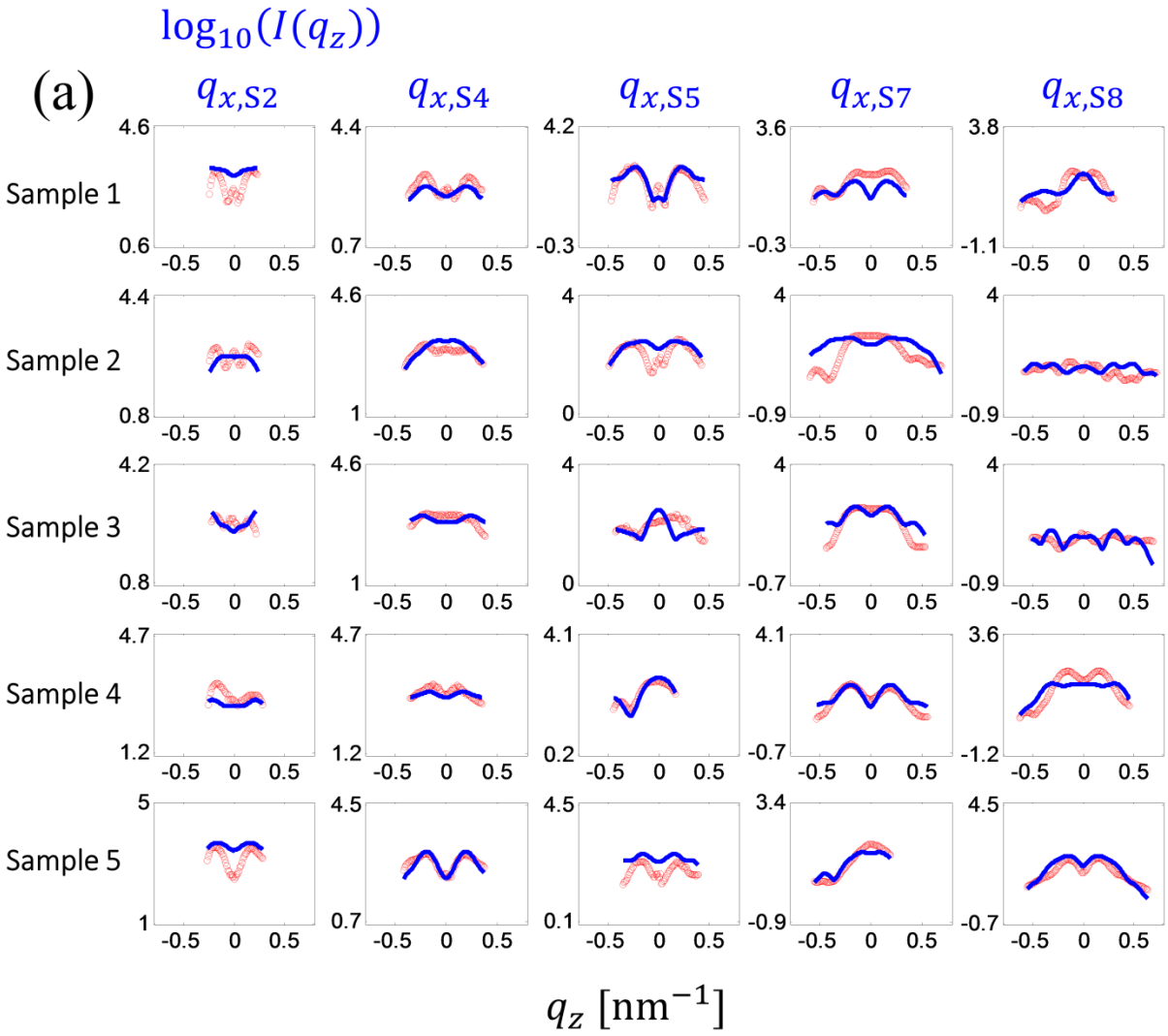

Figure S5a: Intensity profiles for the five samples with increasing guide stripe width from top to bottom where the red circles are the experimental data and the blue lines are the satellite peak slice fits.

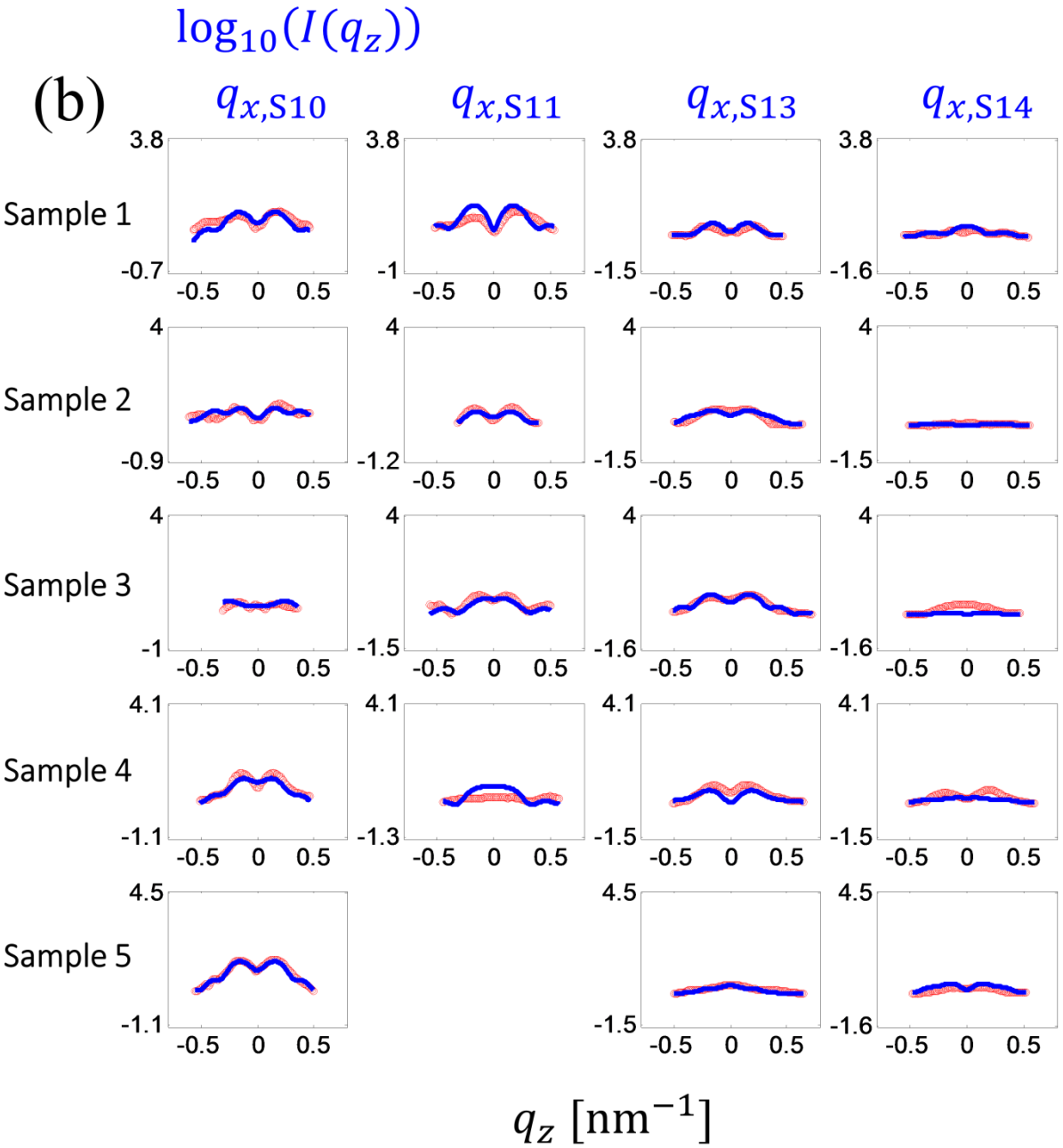

Figure S5b: Intensity profiles for the five samples with increasing guide stripe width from top to bottom where the red circles are the experimental data and the blue lines are the satellite peak slice fits.

Table S2 lists all the best fit model parameters for the five samples using model 3 from the main text (analogous to Table 1 in the main text).

Parameter	Sample 1	Sample 2	Sample 3	Sample 4	Sample 5	Bounds
f	0.47					Fixed
χN	16.5 ± 0.7	13.6 ± 1.1	15.0 ± 0.8	17.6 ± 0.4	17.9 ± 0.4	12.0: 30.0
$L_0/L_{0,\mathrm{SSL}}$	0.76 ± 0.07	0.84 ± 0.03	0.76 ± 0.01	0.73 ± 0.01	0.81 ± 0.05	0.60: 1.10
t_{Film}/L_0	1.26 ± 0.12	1.47 ± 0.06	1.38 ± 0.01	1.33 ± 0.01	1.53 ± 0.04	1.20: 1.60
Ω_{GS}	-9.9 ± 1.8	-3.2 ± 0.2	-3.3 ± 0.4	-4.7 ± 0.6	-2.00 ± 0.05	−15.0: −2.0
Ω_{Air}	-1.20 ± 0.12	-0.52 ± 0.05	-0.85 ± 0.05	-2.0 ± 0.3	-1.2 ± 0.3	−8.0: −0.5
Ω_{Br}	-1.55 ± 0.12	-1.5 ± 0.5	-1.33 ± 0.06	-0.90 ± 0.08	-6.3 ± 1.7	−8.0: −0.5
Ω_{SW}	6.2 ± 0.2	12.1 ± 1.1	14.44 ± 0.09	5.8 ± 3.4	8.5 ± 0.9	2.0: 15.0
L_{GS}/L_0	0.27 ± 0.19	0.87 ± 0.19	0.73 ± 0.38	0.73 ± 0.38	1.20 ± 0.19	0.20: 1.30
L_{Bot}/L_0	1.00 ± 0.04	1.6 ± 0.4	2.2 ± 0.2	2.2 ± 0.3	1.93 ± 0.04	0.20: 2.50
t_{GS}/L_0	0.40					Fixed
t_{Br}/L_0	0.27					Fixed
b [nm]	0.81 ± 0.01	0.74 ± 0.02	0.77 ± 0.01	0.85 ± 0.01	0.89 ± 0.01	0.50: 2.00
DW [nm]	2.20 ± 0.03	2.27 ± 0.06	2.21 ± 0.02	2.22 ± 0.03	2.30 ± 0.02	0.03: 9.90
I_{Exp}	-0.87 ± 0.04	-1.00 ± 0.06	-0.85 ± 0.05	-0.87 ± 0.04	-1.11 ± 0.04	−1.57: −0.57
I_{Bk}	0.62 ± 0.02	0.81 ± 0.05	0.63 ± 0.02	0.89 ± 0.02	0.81 ± 0.04	0.11: 0.90
	Goodness of Fit					
Ξ	0.206 ± 0.027	0.222 ± 0.027	0.167 ± 0.019	0.209 ± 0.003	0.194 ± 0.005	

Table S2: (Top) Parameter values and their fit uncertainty for the five different samples for the best fits found to the set of experimental data using the fully complex template model. (Bottom) The corresponding Ξ goodness of fit values for the five different samples. Uncertainty values are averaged from the 5 best fits. (Right) Parameter search bounds for the given parameter.

ESI4 TICG and SCFT Model Fit Parameter Discussion

Figure S6 compares the main parameters for the 5 samples with those found via the TICG model[6]. The L_{GS} parameter generally increased for both models, with sample number as expected from the SEM measured values. It is of interest to consider the effect of allowing the stripe bounds to be larger, to explore how well the algorithm could converge to the expected value. Doing this allows the technique to be used more as a predictive tool (in cases where there may not be additional measurements to constrain parameters). A similar approach was followed for the film thickness. Supplemental ellipsometry measurements were used to tightly constrain t_{Film} in the TICG study, while wider bounds were used here with the SCFT model to try to predict the film thickness. This resulted in lower and more varied t_{Film} values for the best fits with the SCFT model.

The TICG model did not vary L_{Bot} explicitly but instead varied the angle θ_{SW} between the bottom of the trapezoid and the sidewall. Thus, to compare the found parameters, θ_{SW} was converted to L_{Bot} according to Eqn S12 as

$$L_{\mathrm{Bot}} = L_{\mathrm{GS}} + 2t_{\mathrm{Film}}/\tan\theta_{\mathrm{SW}}. \quad \text{(S12)}$$

This equation was similarly used to convert the search bounds of θ from 20° to 35° to the bounds shown in Figure S6. Such a conversion involved looking at the maximum and minimum bounds for L_{GS} and t_{Film} as well, thus explaining the very large search bounds for L_{Bot} for the TICG model.

In the TICG model, the χN values found cannot be directly compared with those of the SCFT model since the TICG model has a finite non-zero interaction range and considers fluctuation effects. Thus, to compare these values, the TICG model parameters can be converted to an effective value χN_{eff} as described in previous work[7] by estimating the mean-field limit value from an intermolecular pair correlation function and semi-grand canonical equation of state. The previous work did this estimation for a chain size of 32 beads (the same number used in the TICG CDSAXS study[6]) as a function of n_{Int}, the average number of particles with which a given particle interacts. This results in a ratio of $(\chi N_{\mathrm{eff}})/(\chi N) = f(n_{\mathrm{Int}})$ which is plotted in the first figure of the previous work[7]. For $n_{\mathrm{Int}} = 14$ which is the case in the TICG CDSAXS study, this ratio is $(\chi N_{\mathrm{eff}})/(\chi N) \cong 0.82$. In general, the χN values found in the TICG model were larger than the SCFT values. This discrepancy is possibly related to the fact that a binary SLD was used from the resulting SCFT densities for the intensity calculations. However, to be most comparable with the previous trapezoid shape model studies, a binary SLD with DW was necessary. Thus, the χ values found are instead more dependent on the interfacial width model used in relating χ and b to DW than the pure SCFT model used. The TICG model calculations instead averaged in reciprocal space many fluctuation density profile contributions, which should leave a stronger dependence on χ in the calculated data than the SCFT model. The last parameter compared, the interface width w_{Int}, was calculated parameter in both models (from the DW parameter in the SCFT model and from χ using the model given in prior work[1,7]) and thus calculated search bounds were very wide in both models, so those are not shown in Figure S6. However, both models showed values very close to 5 nm, a value previously reported for the bulk PS-*b*-PMMA systems[8–11] with the SCFT model slightly larger than the TICG model. The results for the interface width in the SCFT model are of course only valid if the model used is

correct, but seeing that the values found are approximately in agreement with previous results this seems reasonable. The w_{Int} values for the SCFT model were always larger than those for the TICG model; these observation indicates that the way in which the interface model was used in the SCFT case, where thermal fluctuations were not considered and therefore do not contribute to interfacial fluctuations, has an effect on the interfacial width values that emerge from the fitting process.

Other parameters examined by both models include the t_{Br}/L_0 which was fixed in the TICG to 0.286 and found to be around 0.27 in the SCFT for all samples and the t_{GS}/L_0 was found with an average value of 0.33 in the TICG and 0.40 in the SCFT model. The larger value for t_{GS} found in the SCFT model might be due to the SCFT model finding lower t_{Film} with a possible correlation in those parameters. Another possibility is that the guide stripe has no contrast with the PS layer due to the same SLD values being used and thus more uncertainty exists with that parameter in general. The chemical surface affinities for the sidewall, guide stripe, brush layer, and air interfaces cannot directly be compared between the two models as χ interaction parameters were used to model the surface affinities in the TICG model while the SCFT model used fixed chemical potential energies at those interfaces instead.

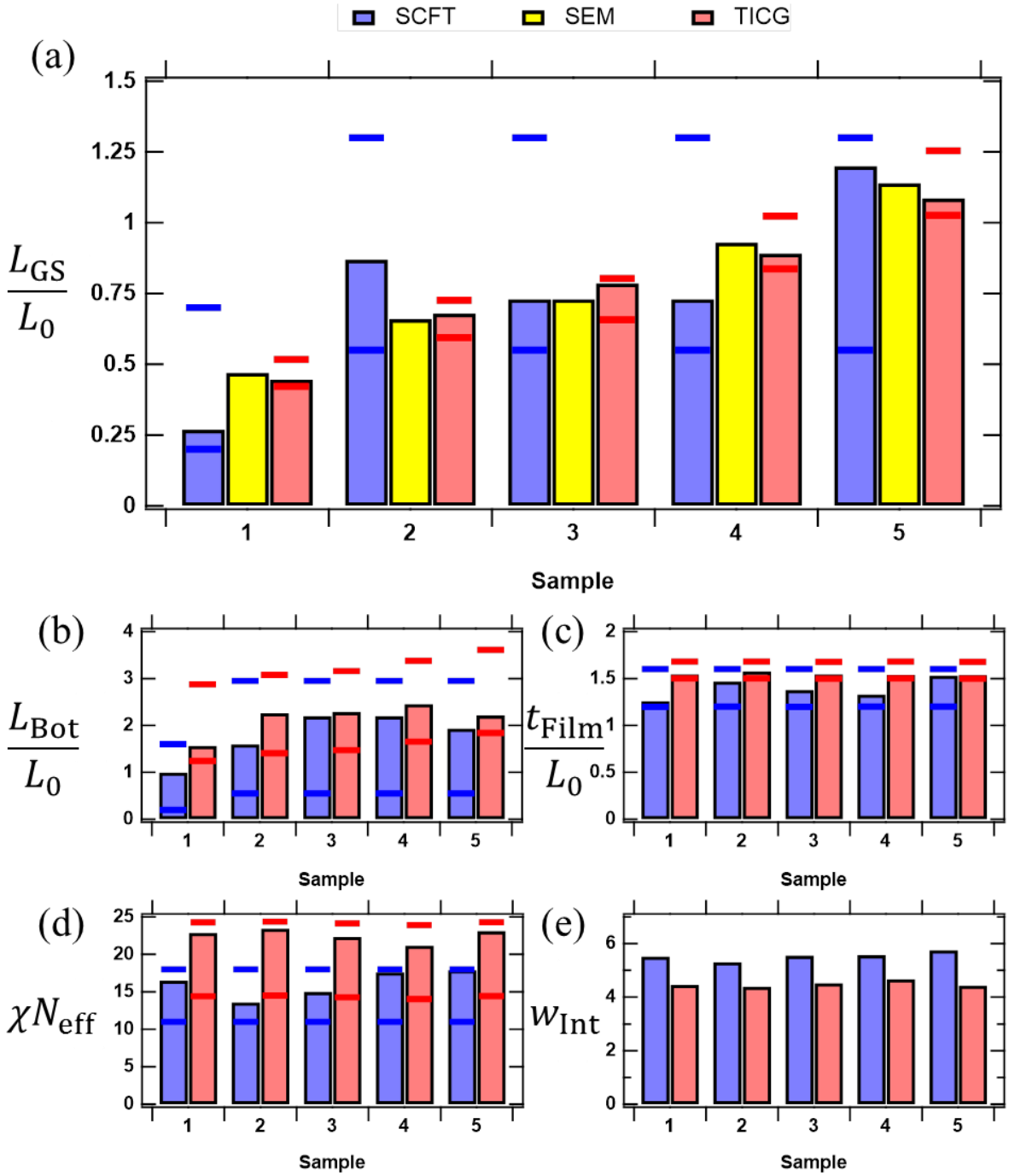

Figure S6: Comparison plots of the parameters found from different models with range bars showing the parameter search bounds where applicable (SCFT in blue and TICG in red) and SEM measurements (yellow) for the L_{GS}/L_0 parameter. (a) L_{GS}/L_0 for all 5 samples with search bounds for SCFT and TICG and SEM measurements for comparison. (b) L_{Bot}/L_0 for all 5 samples with search bounds for SCFT and TICG. (c) t_{Film}/L_0 for all 5 samples with search bounds for SCFT and TICG. (d) χN_{eff} for all 5 samples with search bounds for SCFT and TICG. (e) w_{Int} in nm for all 5 samples. No search bounds are given for w_{Int} since it is a calculated parameter.

ESI5 Future Model Enhancements

Several aspects of the model can still be enhanced, based on its observed inability to exactly determine the guide stripe width apart from the BCP shape profile, as well as the grid based shape model getting lower Ξ values for the goodness of fit for most samples. The guide stripe and brush regions were modeled with simple hard mask regions, while more advanced models could explicitly model them as X-PS and a random brush layer, respectively. With such a model, some way to have the model explicitly distinguish the X-PS region from the PS region may be necessary. The air surface interface is most likely not flat as modeled, so including an air shape parameter would likely enhance the model as well. Fluctuation effects were not considered explicitly as the density profiles used to calculate the SLD were the mean field relaxed solutions (this is different from local compositional fluctuations due to the finite simulation time and initial random noise added to the seeded field guess solution), thus methods probing fluctuation effects may find better fits if the fluctuation of the structure is contributing to the scattered intensity profile. There could also be potential effects in 3D structure that may affect some of the shape; however, additional q_y data would be necessary to make a full 3D SCFT study viable.

ESI References

1 A. N. Semenov, *Macromolecules*, 1993, **26**, 6617–6621.

2 M. W. Matsen and F. S. Bates, *Macromolecules*, 1996, **29**, 1091–1098.

3 D. F. Sunday, M. R. Hammond, C. Wang, W. L. Wu, D. M. Delongchamp, M. Tjio, J. Y. Cheng, J. W. Pitera and R. J. Kline, *ACS Nano*, 2014, **8**, 8426–8437.

4 D. F. Sunday, M. R. Hammond, C. Wang, W. Wu, R. J. Kline and G. E. Stein, *J. Micro/Nanolithography, MEMS, MOEMS*, 2013, **12**, 031103.

5 A. F. Hannon, D. F. Sunday, D. Windover and R. Joseph Kline, *J. Micro/Nanolithography, MEMS, MOEMS*, 2016, **15**, 034001.

6 G. Khaira, M. Doxastakis, A. Bowen, J. Ren, H. S. Suh, T. Segal-Peretz, X. Chen, C. Zhou, A. F. Hannon, N. J. Ferrier, V. Vishwanath, D. F. Sunday, R. Gronheid, R. J. Kline, J. J. de Pablo and P. F. Nealey, *Macromolecules*, 2017, **50**, 7783–7793.

7 D. Q. Pike, F. A. Detcheverry, M. Müller and J. J. De Pablo, *J. Chem. Phys.*, , DOI:10.1063/1.3187936.

8 S. H. Anastasiadis, T. P. Russell, S. K. Satija and C. F. Majkrzak, *J. Chem. Phys.*, 1990, **92**, 5677–5691.

9 T. P. Russell, A. Menelle, W. A. Hamilton, G. S. Smith, S. K. Satija and C. F. Majkrzak, *Macromolecules*, 1991, **24**, 5721–5726.

10 P. Ramya, C. Ranganathaiah and J. F. Williams, *Polymer*, 2012, **53**, 4539–4546.

11 D. F. Sunday and R. J. Kline, *Macromolecules*, 2015, **48**, 679–686.